



COMMUNICATIONS PHYSICS

ARTICLE

DOI: 10.1038/s42005-018-0034-3

OPEN

Spontaneous light-mediated magnetism in cold atoms

I. Krešić^{1,2}, G. Labeyrie³, G.R.M. Robb¹, G.-L. Oppo¹, P.M. Gomes¹, P. Griffin¹, R. Kaiser³ & T. Ackemann¹

Cold atom setups are now commonly employed in simulations of condensed matter phenomena. We present an approach to induce strong magnetic interactions between atoms on a self-organized lattice using diffraction of light. Diffractive propagation of structured light fields leads to an exchange between phase and amplitude modulated planes which can be used to couple atomic degrees of freedom via optical pumping nonlinearities. In the experiment a cold cloud of Rb atoms placed near a retro-reflecting mirror is driven by a detuned pump laser. We demonstrate spontaneous magnetic ordering in the Zeeman sub-levels of the atomic ground state: anti-ferromagnetic structures on a square lattice and ferrimagnetic structures on a hexagonal lattice in zero and a weak longitudinal magnetic field, respectively. The ordered state is destroyed by a transverse magnetic field via coherent dynamics. A connection to the transverse (quantum) Ising model is drawn.

¹SUPA and Department of Physics, University of Strathclyde, Glasgow G4 0NG Scotland, UK. ²Institute of Physics, Bijenička cesta 46, 10000 Zagreb, Croatia. ³Université Côte d'Azur, CNRS, Institut de Physique de Nice, 1361 Route des Lucioles, 06560 Valbonne, France. Correspondence and requests for materials should be addressed to T.A. (email: thorsten.ackemann@strath.ac.uk)

Improving the understanding of magnetic interactions is of paramount importance due to the challenges associated with exotic magnetic phenomena, the potential connections to high-Tc superconductivity, and the widespread use of magnetic materials in current technology. A popular approach is to develop relatively simple, controllable “quantum simulators” of magnetic interactions using ultracold atoms loaded in optical lattices¹. These simulators have been used to investigate classical² and quantum^{3–7} magnetism, including the role played by the range of the spin-interaction^{8–11}. Without externally applied optical lattices, spontaneous magnetization of spinor condensates^{12–14} has been observed. Magnetic coupling between atoms is obtained via artificial gauge fields^{15,16} or via dipole-dipole interaction of polar molecules¹⁷, highly magnetic atoms¹⁸, and Rydberg atoms^{5,9,10}. Here we provide an alternative approach where spin-spin interactions in a cold atomic gas are mediated through light over length scales determined by diffractive dephasing. We demonstrate antiferromagnetic and ferrimagnetic phases. Transitions between magnetic phases are induced by external magnetic fields in close connection to the transverse (quantum) Ising model^{19–26}.

Results

Diffractive coupling scheme and experimental setup. The matter density in ensembles of laser-cooled thermal atoms is typically too low to observe direct magnetic interactions between atoms in different Zeeman states. In our experiment, however, strong interactions and magnetic ordering are mediated through state-selective optical nonlinearities combined with diffractive light propagation in a feedback scheme as sketched in Fig. 1a²⁷. A 100–200 μK cold atomic cloud is illuminated by a pump laser beam propagating along z and linearly-polarized along x . The transmitted beam is retro-reflected by a semi-transparent mirror ($R > 95\%$) located at a distance d behind the cloud. The beam is detuned from the atomic transition by several linewidths such that single-pass absorption is moderate and the nonlinear effects described here are mainly dispersive in character. Under these conditions a spatial modulation of a state variable in the atomic system at a transverse wavenumber q will impart a phase modulation on the transmitted light. Diffractive dephasing in the feedback loop results in conversion of phase to amplitude modulations. This conversion is related to the Talbot effect²⁸, a self-imaging effect for periodic light structures. The phase between the

generated sidebands at q and the pump varies as $\exp(iq^2z/(2k))$ (k wavenumber of light) under the paraxial approximation. Hence for a wavenumber with $\exp(iq^2(2d)/(2k)) = i$ the initial phase modulation is converted to an amplitude modulation for the reentrant field, which can provide positive feedback to the original fluctuation for a self-focusing situation in which the phase (or refractive index) increases with intensity. This provides the light-mediated coupling in our experiment. The spatial period for the ordered magnetization state is given by $\Lambda = \sqrt{4\lambda d}$ ²⁷. The emerging spatial structure spontaneously breaks the translational and rotational symmetry in the $x-y$ -plane transverse to the pump axis. This is similar to the symmetry breaking in multi-mode cavities^{29,30}, but different from transversely pumped single-mode cavities^{31–34} in which the symmetry and orientation of the spatial structures is determined by the pump and cavity axis. For cold quasi-2-level atoms in non-cavity schemes, the spontaneous emergence of ordered structures was demonstrated previously in experiments using either opto-mechanical nonlinearities due to the dipole force³⁵ or Sisyphus cooling-assisted bunching^{36,37} or inversion patterns due to the saturation of the atomic transition³⁸.

In order to produce magnetic ordering, the magnetic substructure of the atomic states can be exploited. The experiment is performed on the $F=2 \rightarrow F'=3$ transition of the D2 line of ⁸⁷Rb, but the simpler $F=1 \rightarrow F'=2$ transition (Fig. 1b) is sufficient to explain the observed features. Choosing the quantization axis along z , the pump beam axis, the interaction is described in terms of circularly polarized light components, σ^+ and σ^- . When a low saturation parameter is employed, the optical properties of the gas are determined by the magnetization in the ground state. This contains magnetic dipole and quadrupole contributions which can be written in terms of the density matrix elements ρ_{ij} . Here we focus on the magnetic spin $w = \rho_{11} - \rho_{-1,-1}$, which corresponds to a magnetic dipole in the z -direction. It is produced by pumping with an optical beam possessing a net spin, i.e. a non-zero circular polarization component. The σ^+ (resp. σ^-) component induces population transfer toward the stretched state $m_F = +1$ (resp. $m_F = -1$) known as Zeeman pumping (Fig. 1b). In zero magnetic field, this process is described by

$$\dot{w} = -\Gamma_w w + \frac{5}{18} D + \text{higher order multipoles}, \quad (1)$$

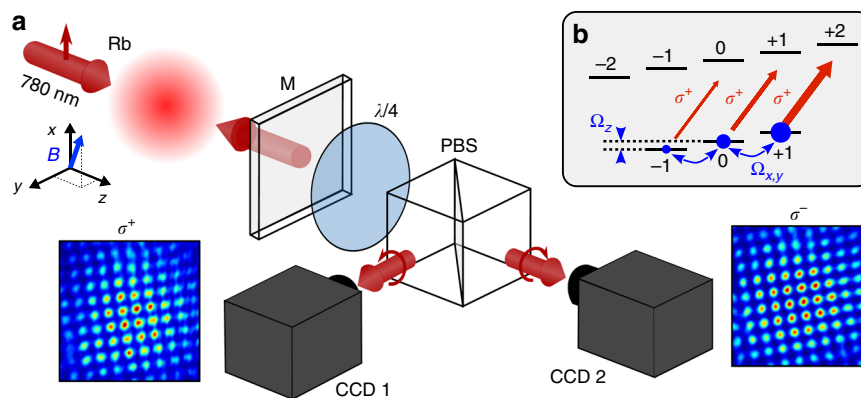


Fig. 1 Principle of experiment. **a** Schematic setup and scheme of pattern detection providing near field images projected on circular polarization states. M - plane mirror with $R \approx 0.95$, $\lambda/4$ quarter-wave plate, PBS polarizing beam splitter cube, CCD charge-coupled device camera. The clockwise/counter-clockwise arrows indicate the helicity monitored in the respective detection arms, the beams are linearly polarized after the PBS. **b** Level scheme of $F=1 \rightarrow F'=2$ transition illustrating Zeeman pumping with circularly polarized light between Zeeman sub-levels with magnetic quantum numbers m_F . A longitudinal magnetic field with Larmor frequency Ω_z removes the degeneracy between Zeeman states, a transverse field with Larmor frequency $\Omega_{x,y}$ couples them coherently. The population difference between the $m_F = 1$ and $m_F = -1$ levels represents an orientation or magnetic dipole oriented in z -direction

where $D = P_+ - P_-$ is the difference pump rate between the σ_{\pm} -components (each being characterized by a pump rate $P_{\pm} \sim |E_{\pm}|^2$) and $\Gamma_w = r + S/6$ describes relaxation, r being an effective relaxation rate due to atomic motion and $S = P_+ + P_-$ the sum of the pump rates. The latter saturation term ensures that the spin orientation remains bounded.

As indicated, we concentrate on the interaction of the optical spin with the atomic dipole moment (tensor rank 1 of irreducible tensor components³⁹). The $F=2$ ground state used in the experiment and the $F=1$ ground state used in the modeling allow for higher moments, in principle. A linearly polarized pump field will not induce an orientation but will induce alignment components (magnetic quadrupoles) $X = \rho_{11} + \rho_{-1-1} - 2\rho_{00}$ and $\Delta m = 2$ coherences $\Phi = 2\rho_{1-1} = u + iv$. Effects of these are under current investigation. For the full equations, we refer to Eqs. (8a)–(8l) of the Supplementary Note 1. It is important to stress that the magnetic fields induce coherent coupling within the dipole and quadrupole components but not between dipole and quadrupole components⁴⁰, enabling us to treat the ordering of the dipole magnetization separately from the more complex atomic states to a large extent. The homogeneous quadrupole components are important on a quantitative level and responsible for symmetry breaking (see below) but they are not driving the magnetic ordering discussed here.

The action of the atomic orientation (spin) pattern on the optical spin structure, i.e. the circularly-polarized optical fields E_{\pm} , is described by

$$\frac{\partial}{\partial z} E_{\pm} = -i \frac{k\chi_{\pm}}{2} \left[\left(1 \pm \frac{3}{4} w \right) E_{\pm} + \text{higher order multipoles} \right]. \quad (2)$$

Here, $\chi_{\pm} = -b_0/(kL) \times [2\Gamma(\delta \mp \Omega_z)]/[\Gamma^2 + 4(\delta \mp \Omega_z)^2]$ is the linear susceptibility, where δ denotes the detuning, Γ the radiative decay rate of the transition, b_0 the optical density at line center, L the medium length, and Ω_z the Larmor frequency of the B-field in z -direction. In zero magnetic field, the linearly polarized pump field alone will not induce an orientation. As long as the spin system $w(x, y)$ in the atomic cloud is disordered, the difference pump rate D of the fed back E_{\pm} -fields is disordered, too. A localized (Fig. 2a) or periodic modulation (Fig. 2b, c lowest subpanel) will instead generate opposite modulations of phase shifts for the σ_{\pm} components (see the $\pm w$ in Eq. (2), Fig. 2c central two subpanels) and, due to the diffractive phase-shifts in the feedback loop, a spatial separation of the σ_{\pm} components arises (Fig. 2c uppermost subpanel). A self-organized optical spin pattern is then generated in the backward field reentering the cloud. The resulting non-zero difference pump rate, D , will drive the atomic spin ordering via Eq. (1). As the propagation time of the light field is much shorter than the time scales of the atomic dynamics, the ordering can be interpreted as to arise from an interaction of atoms in separate Zeeman states via light-mediated coupling. For $F = 1/2 \rightarrow F' = 1/2$ -transitions, a related instability is known in hot atomic vapors^{41–46}, but these studies focused on the nonlinear optics aspects of the self-organization.

Polarization aspects were also investigated in the transverse instability occurring in counterpropagating beams in a nonlinear optical medium, although these studies focused on optical wave-mixing^{47–53}. The counterpropagating beam instability is linked to the single-mirror feedback instability but requires a simultaneous treatment of diffraction and nonlinearity. If in a single-mirror setup the mirror position is in the medium, the threshold increases and the length scale does not decrease any more like

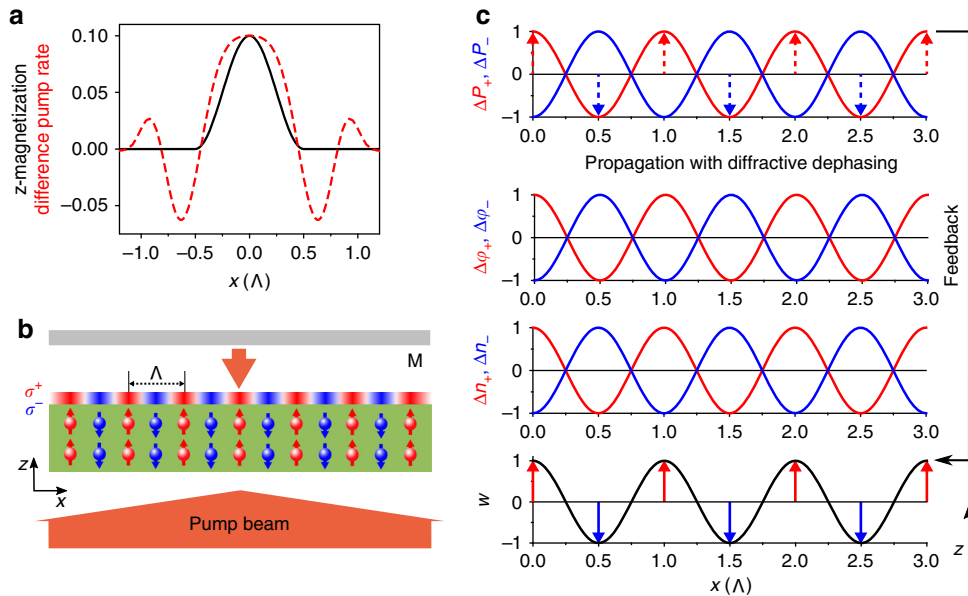


Fig. 2 Light-mediated coupling. **a** A localized perturbation of the z -magnetization w (solid black line) will lead to a difference pump rate D (dashed red line) which enhances the original perturbation around $x \approx 0$, pumps into the anti-parallel direction providing antiferromagnetic coupling about half a lattice period away ($x \approx \pm 0.5$, the transverse space coordinate is scaled to the lattice period Λ) and pumps into the parallel direction providing ferromagnetic coupling about one lattice period away ($x \approx \pm 1$). The result is an Ising-like antiferromagnetic coupling of super-spins (see text) centered on the lattice sites. (The input pump rate is adjusted for display purposes such that the magnetization and difference pump rate have equal peak amplitude.) **b** Above threshold, the asymptotic ordered magnetic state is sustained via an optical spin pattern induced, in turn, via diffraction of the transmitted light. **c** Detailed explanation of mechanism of spin ordering: A spatial modulation in the orientation w changes the refractive index for the σ^+ , σ^- -components in an opposite direction and hence after the atomic cloud the circular components of the pump acquire an opposite modulation of phase shifts (see Eq. (2)). After propagation in the feedback loop, the resulting amplitude modulations are also opposite. The resulting optical spin structure can then sustain the atomic orientation. Red arrows: Spin-up super-spins, blue arrows: spin-down super-spins, solid arrows: atomic super-spins, dashed arrows: corresponding super-spin of photon helicity

$\sqrt{\lambda d}$ but is limited to slightly larger than $\sqrt{\lambda L}$, where L is the medium length, as a new significant diffractive length⁵⁴. In our experiment, the mirror is typically placed just outside the cloud to reduce these effects, but close enough to the cloud to maximize the number of lattice sites within the pump beam by being close to the minimum lattice period. The resulting scale for the pattern period is about $\Lambda \approx 100 \mu\text{m}$ for the Nice experiment and $\Lambda \approx 50 \mu\text{m}$ for the Strathclyde experiment. The control of the position of the mirror is achieved via an imaging system (see ‘Experimental Details’ in the Methods Section) and hence can be both positive and negative.

Ising-like interaction. Figure 2a illustrates that the spatial structure of the difference pump rate fed back supports an Ising-like interaction mechanism for the atomic spins on the lattice created by the instability which is much bigger than typical atomic separations. A perturbation of w ranging over half of the self-organized lattice period creates an optical spin structure that enhances the magnetization at the point of perturbation and at locations one period away (the nearest neighbors) but will also lead to negative, i.e. antiferromagnetic, coupling at half the period. This ferromagnetic, respectively antiferromagnetic, coupling increases with optical density and input intensity. For a harmonic perturbation $w = \delta w \cos(qx)$ a simple relation for the amplitude of the difference pump rate δD can be derived by a linear

expansion of Eqs. (1) and (2),

$$\delta D = -3P_0\phi_0\delta w, \quad (3)$$

where $\phi_0 = b_0\delta/\Gamma/[1 + 4(\delta/\Gamma)^2]$ is the linear phase shift. For a localized perturbation like in Fig. 2a or general distributions there is no simple closed expression but the scalings hold, i.e. the interaction strength is given by the dispersive optical density (i.e. the linear phase shift) and the pump rate. The question whether it is possible to derive an effective Hamiltonian for the super-spins describing the dynamics of an open quantum system is open at this stage of investigations.

Observation of antiferromagnetic ordering. For an observation of magnetic ordering, we typically set the laser detuning at a value of δ between -7Γ and -9Γ . The laser intensity used is as low as 1 mW/cm^2 , typically two orders of magnitude below non-magnetic instability thresholds^{35,38}. Under these conditions, square lattices of large domains of spin-oriented atoms are observed in the near-field (NF) as can be seen in Figs. 1 and 3a,b. The two square lattices detected in the σ^+ and σ^- channels are interlaced, as illustrated in Fig. 3c, where the NF intensity difference $I(\sigma^+) - I(\sigma^-)$ is plotted. This difference is an indicator of the orientation distribution, $w(x, y)$. The plot in Fig. 3e corresponds to a cut of the experimental intensity difference image along the dashed line, and emphasizes the periodic, symmetrical arrangement in zones

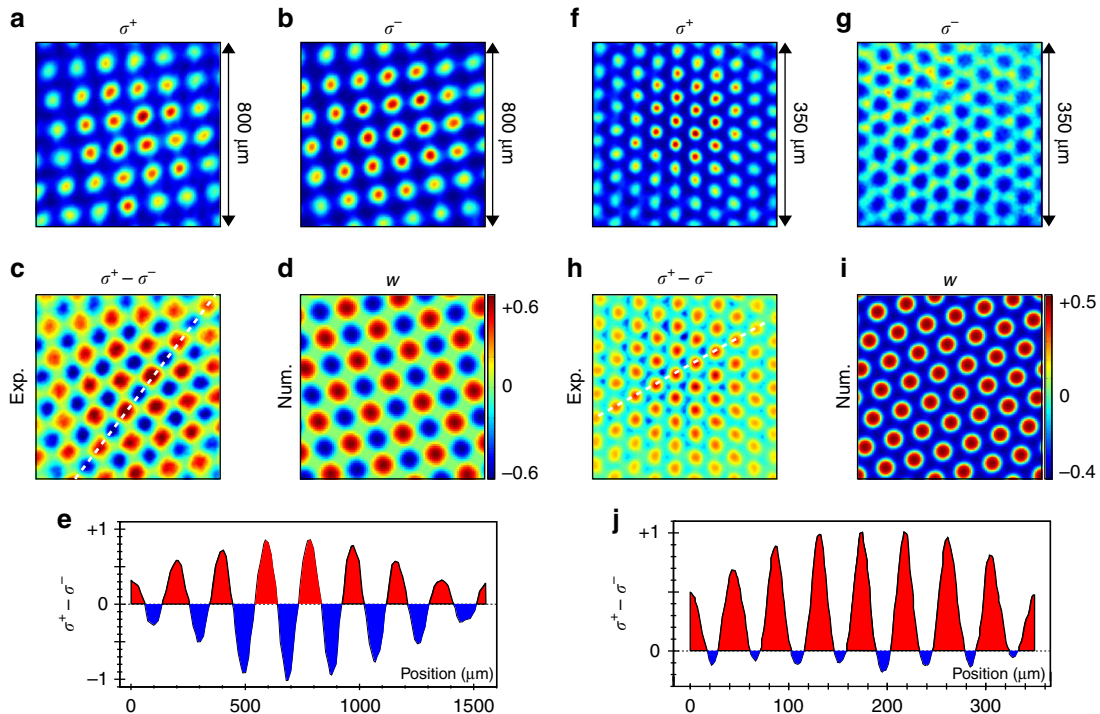


Fig. 3 Observed magnetic structures. Spontaneous antiferromagnetic (a–e) and ferrimagnetic (f–j) phases for $B_x = B_y = 0$. We show examples from both experiments. **a, b** NF intensity of the σ^+ and σ^- components for $B_z = 0$. Nice experiment: $b_0 = 80$, $\delta = -8\Gamma$, $I = 10 \text{ mW/cm}^2$, $d = -20 \text{ mm}$. **f, g** NF intensity of the σ^+ and σ^- components for $B_z \neq 0$. Strathclyde experiment: $b_0 = 27$, $\delta = -7\Gamma$, $I = 10 \text{ mW/cm}^2$, $B_z = 120 \text{ mG}$, $d = -2.9 \text{ mm}$. **c, h** NF intensity difference of the σ^+ and σ^- components for $B_z = 0$ and $B_z \neq 0$, respectively. **d, i** Spatial structure of the orientation w obtained from numerical integration of Eqs. (8a)–(8d) of the Supplementary Note 1 for $B_z = 0$ and $B_z \neq 0$, respectively. **e, j** 1D cut of the NF intensity difference of the σ^+ and σ^- components along the dotted lines of **c, h** for $B_z = 0$ and $B_z \neq 0$, respectively. The structures in **a** and **b** are scaled in the same way, as are the ones in **f, g**. In **c, h** the maximum absolute value of the minimum and maximum of each difference image is taken to normalize the difference to a value between -1 and 1 . This is indicative of the orientation structure w . In this normalization, the scale bars for the numerical w distribution are also indicative for the interpretation of the experimental difference image, i.e. indicate where zero magnetization is and the relative size of the positive/negative excursions. The normalized plot is chosen as it is not very reliable to connect the absolute amplitude to an absolute magnetization. Typical values of magnetic field in which hexagonally coordinated ferrimagnetic structures are obtained are $B_z \approx 50 \dots 150 \text{ mG}$, details depending on values of detuning, optical density and in particular input intensity (see Methods ‘Symmetry breaking in a longitudinal magnetic field’)

of opposite light helicity. This structure corresponds to an anti-ferromagnetic phase. Indeed, for $B_z = 0$, there is no Zeeman splitting and the system is fully symmetric for the σ^+ and σ^- light components. Spontaneous symmetry breaking leads to an anti-ferromagnetic state with zero net magnetization and an arbitrary spatial phase. This analysis is confirmed by numerical simulations which solve the coupled equations for the light field and atomic variables in the presence of mirror feedback, Eqs. (8a)–(8d) of the Supplementary Note 1. The computed transverse spatial distribution of w is shown in Fig. 3d. The corresponding $I(\sigma^+) - I(\sigma^-)$ image (not shown) closely matches the experimental data.

The spin-oriented domains have similar size and contain a large number of atomic spins. A macroscopic orientation (super-spin) can be obtained by averaging over the atomic spins in each domain and by assigning positive or negative magnetization to the corresponding lattice points at the period of the w lattice. The macroscopic super-spins at each lattice point will then interact with their neighboring lattice spins via diffracted light (Fig. 2a), sustaining the anti-ferromagnetic ordering. Consequently this corresponds to a simulator of interacting semiclassical spins made of domains of spin-oriented cold atoms. We observe shot-to-shot fluctuations of both orientation and position of the structures between different realizations, as expected from the continuous symmetries that are spontaneously broken (translation and rotation in the transverse plane). Patterns can also include defects, deformations or irregularities of amplitudes.

Observation of ferrimagnetic ordering. When a longitudinal magnetic field B_z is applied, a further symmetry breaking occurs, leading to a preferred sign of the orientation. However, for a small field B_z the anti-ferromagnetic square pattern survives, in accordance with the anti-ferromagnetic Ising model in a longitudinal field²³. Increasing the B_z field to about 0.1 G we observe a transition from square (anti-ferromagnetic) to hexagonal (ferrimagnetic) lattices, as shown in Fig. 3f–h, j. The ferrimagnetic state exhibits striking differences between the two polarization channels, with hexagonally coordinated peaks in one component and honeycombs in the other (Fig. 3f, g). These are still interleaved with each other but the amplitudes of the components are very different as shown in Fig. 3h, j through the $I_{\sigma^+} - I_{\sigma^-}$ image. The 1D cut of this experimental image shows that the spins on the hexagonal lattice are mostly oriented along one direction, with only $\approx 10\%$ of them in the opposite direction. This is a ferrimagnetic phase. The simulations show the corresponding spatial modulation of w in Fig. 3i. By flipping the sign of B_z , the roles of σ^+ and σ^- are exchanged and the sign of the dominant magnetization inverted in response to the inversion symmetry breaking by the external field.

The transition from square to hexagonal structures can be understood using a symmetry argument^{55–57}. In the absence of an inversion symmetry (e.g. when $B_z \neq 0$) pattern selection is governed by quadratic interactions allowing three-wave mixing. This favors hexagonal patterns as the sum of two lattice wavevectors will yield a vector with the lattice wavenumber only for an angle of 120° . Other kinds of lattices (including squares) can emerge if inversion symmetry is respected ($B_z = 0$). Note also that an anti-ferromagnetic state cannot exist on a triangular (and thus hexagonal) lattice as this would lead to frustration^{2,58}. Increasing the B_z -field it is observed that the clear hexagonal symmetry is destroyed and disordered spin patterns prevail. This transition is currently investigated in more detail. Symmetry breaking due to a longitudinal field occurs in standard anti-ferromagnetic Ising models but to an unstructured, paramagnetic state²². This paramagnetic phase is outside the capability of our current apparatus, but is expected for larger B-

fields (several Gauss) such that $\Omega_z \gtrsim \delta$. Transitions to a ferrimagnetic phase occur in models and materials consisting of two layers or two sublattices of magnetic sites^{59–61}. This two layer structure resembles the situation here in which the hexagonally coordinated, dominant super-spins are surrounded by a weaker, opposite magnetization on the ridges of an interleaved honeycomb structure.

Threshold behavior. Figure 4 shows an analysis of the diffracted power at the lattice wavevectors vs. pump. For zero magnetic field (red dots), it evidences a continuous, i.e. second order, transition at a threshold of 4.1 mW/cm^2 to the anti-ferromagnetic state and a linear increase of diffracted power vs. pump intensity beyond threshold. As the diffracted power is proportional to the square of the modulation amplitude of w in linear expansion of Eq. (2), this indicates a square-root scaling of the magnetic order parameter vs. pump above threshold, as expected for the Ising model in mean field limit²⁶ (staggered magnetization for the anti-ferromagnetic case). The transition to the ferrimagnetic hexagonal state at small longitudinal magnetic fields is abrupt, i.e. first order (Fig. 4, blue dots), which is related to the cooperative dynamics due to the breaking of the inversion symmetry as discussed before. For $B_z = 0$ and $r = 2.29 \times 10^{-4} \Gamma_2$, $R = 0.95$ the theory, Eq. (9), indicates a threshold of 0.69 mW/cm^2 neglecting contributions of all other multipoles (i.e. assuming a value of the homogeneous component of the alignment $X_0 = 0$), lower than the experimentally one of 4.1 mW/cm^2 . For a more realistic component of $X_0 = 0.29$ obtained from solving for the homogeneous solution of Eqs. (8a)–(8d) of the Supplementary Note 1 for these parameters, the threshold is 3.5 mW/cm^2 . The remaining differences can be easily explained by the inhomogeneous profile of the Gaussian input beam, transverse stray fields and corrections from the fact that the medium is not really diffractively thin as assumed in this treatment⁵⁴.

Dynamics in transverse fields and transverse Ising model. We now consider the anti-ferromagnetic ordered state when a purely transverse magnetic field is applied. The transverse field stimulates coherent coupling (tunneling) between spin states thus suppressing ordering as described by the transverse (also referred to as the quantum) Ising model^{24–26}. This model shows a quantum phase transition between the ordered anti-ferromagnetic

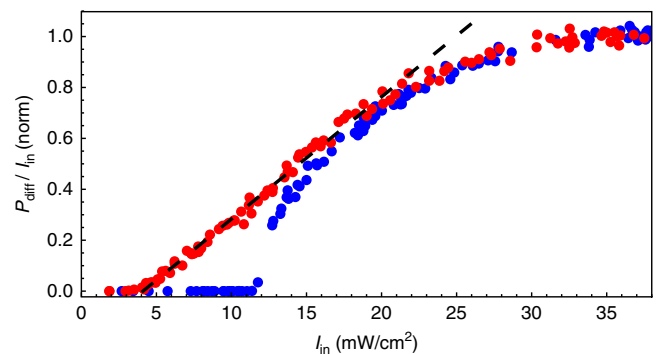


Fig. 4 Threshold behavior. Total diffracted power divided by pump intensity (indicative of the square of the magnetization order parameter) normalized afterwards to its maximum observed value for each of the structures vs. pump intensity. Red dots: anti-ferromagnetic state at $B_z = 0$, blue dots: ferrimagnetic state at $B_z = 130 \text{ mG}$. The dashed black line indicates a linear fit to the linear range of the curve from 4.2 to 21.24 mW cm^{-2} . The threshold extrapolated from the intercept with the x-axis is 4.1 mW cm^{-2} . Other parameters: $b_0 = 27$, $\delta = -7\Gamma$, $d = -2.9 \text{ mm}$ and $B_x \approx B_y \approx 0$

state and a paramagnetic state in which all spins are aligned to the transverse field, even at zero temperature. In our experiment the magnetic coupling induces a phenomenologically similar transition from the antiferromagnet to a state without structure. Figure 5a shows the diffracted power versus the transverse B-field for three different pump values. The diffracted power has an approximately parabolic dependence on the transverse B-field. The maximum diffracted power increases with pump power as does the critical transverse B-field, i.e. the B-field at which the ordered states vanishes, as expected (see Eqs. (11) and (12)). Normalizing the amplitude of the diffracted power to one and the magnetic field to the critical B-field, all the experimental curves fall on an universal parabola (Fig. 5b). As the diffracted power is proportional to the square of the orientation modulation amplitude, the parabola of Fig. 5b corresponds to the magnetization decaying as $\sqrt{1 - (B/B_{\text{crit}})^2}$ in agreement with the transverse Ising model²⁶.

Figure 5c compares the experimentally obtained threshold curve (I_{th} vs. B_y , black squares) with the prediction from Eq. (1) (blue line) incorporating the quantum coupling induced by the transverse field into the relaxation rate Γ_w (see Eq. (7)). The agreement is excellent, except at low magnetic fields. If one allows for a residual stray field of $B_x = 35$ mG (see Methods), the threshold at $B_y \approx 0$ is also reproduced well.

It is important to note that the transverse magnetic field enters the equations as a coherent coupling as in the transverse Ising model^{24–26} as the operator describing the action of a transverse magnetic field does not commute with the z -component of the spin, the orientation w . This provides a coherent decay mechanism of the magnetization, often referred to as quantum tunneling^{24,25}. As the incoherent decay rate is relatively small ($r < 10^4 \text{ s}^{-1}$), the decay dynamics can be easily dominated by coherent spin tunneling via stray and applied transverse fields (Fig. 5c) corresponding to the phase transition in the quantum critical regime at zero and low temperature in the transverse Ising

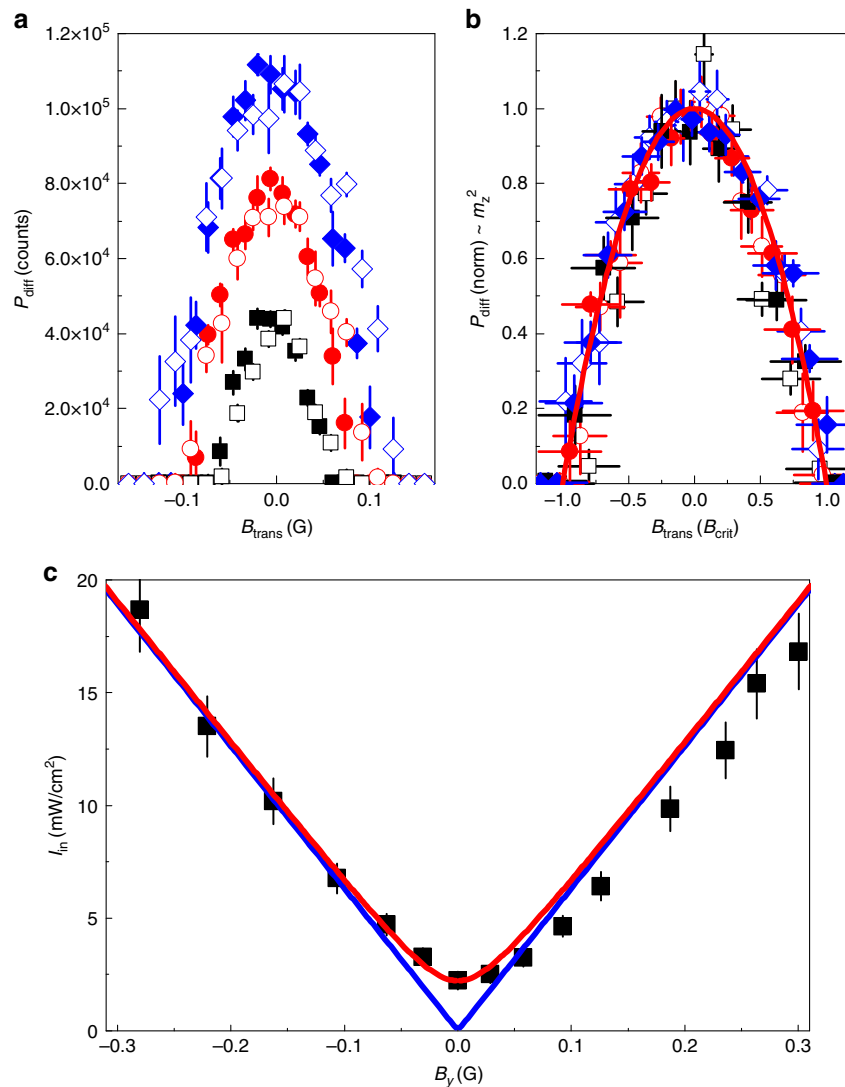


Fig. 5 Suppression of antiferromagnetic magnetic order by transverse magnetic field. **a** Diffracted power in single σ channel at lattice wavenumber detected in far field (Methods) vs. transverse magnetic field strength (solid symbols obtained varying B_x at $B_y = B_z = 0$, open symbols varying B_y at $B_x = B_z = 0$). $b_0 = 27$, $\delta = -7\Gamma$, $d = -4.2$ mm. Black squares for $I_{\text{in}} = 7$ mW/cm². Red circles for $I_{\text{in}} = 10$ mW/cm². Blue rhombs for $I_{\text{in}} = 12$ mW/cm². **b** Normalized diffracted power vs. magnetic field scaled by critical magnetic field (Methods). The red line illustrates the expectation from the transverse Ising model, $m_z^2 = 1 - (B/B_{\text{crit}})^2$. **c** Threshold vs. B_y -field for $b_0 = 80$, $\delta = -8.6\Gamma$, $d = -20$ mm. Black squares: experiment, blue line prediction from Eq. (7) for $r = 2.8 \times 10^3 \text{ s}^{-1}$ and $B_x = 0$, red line considers a stray field of $B_x = 35$ mG. The error bars in **a** derive from the statistics over 10 measurements, the ones in **b** from the uncertainties in scaling and in **c** from an estimation of uncertainty

model. Differently from the transverse Ising model, there is no magnetization without the instability (for $B_z = 0$), so if the spin-flips destroy the z -magnetization, the remaining state is magnetically disordered and not a quantum paramagnet aligned to the transverse field.

Discussion

In conclusion, we demonstrated spontaneous magnetic ordering in a cloud of cold atoms due to light-mediated interactions. The behavior of the system in a longitudinal field is more complex than in the antiferromagnetic Ising model on a single layer as a ferrimagnetic state is obtained after a symmetry breaking transition. The decay of antiferromagnetic order due to quantum tunneling in a transverse magnetic field is also observed in agreement with the transverse Ising model. The role of internal spin temperature is played by the atomic kinetic temperature, but the threshold can be dominated by the quantum tunneling. Hence, this system constitutes a novel, unconventional open system for the study of magnetic ordering on large spatial scales and in a relatively simple cold atom setup. Future investigations consider fluctuations and correlations beyond the semiclassical treatment presented here, e.g. quenching dynamics^{4,62} and fluctuations at the classical-quantum boundary^{63,64}. Of further interest are the influence of frustration in the transition between ferri- and antiferromagnetic order, the existence of magnons and the possibility of optically controllable localized magnetic nucleation domains^{65–67}.

Methods

Experimental details. The results presented in this paper were obtained using two different experimental setups, one in Nice and the other in Strathclyde. Both experiments used a magneto-optical trap (MOT) to prepare a cold cloud (at temperature $T \approx 200 \mu\text{K}$ at Nice, $T \approx 120 \mu\text{K}$ at Strathclyde) of ^{87}Rb atoms. The main difference between the two setups is the number of trapped atoms (10^{11} at Nice and 10^9 at Strathclyde). As a result, both the size L and the optical density (OD) b_0 of the cloud are larger at Nice ($L \approx 14 \text{ mm}$, $b_0 \approx 80$, peak density about $5 \times 10^{10} \text{ cm}^{-3}$) than at Strathclyde ($L \approx 2.6 \text{ mm}$, $b_0 \approx 27$, peak density about $7 \times 10^{10} \text{ cm}^{-3}$).

The threshold for ordering is not given by the spin temperature that is ill-defined since the spins are well isolated from the environment in the vacuum chamber at the low densities employed. The main source of disorder to be overcome is the residual thermal motion of the atoms leading to a wash-out of the spin pattern and thus serving as a kind of effective spin temperature counteracting the magnetic ordering. Typical lattice periods are $\Lambda \gtrsim 100 \mu\text{m}$ (Nice) and $\Lambda \gtrsim 50 \mu\text{m}$ (Strathclyde) giving an estimation of the relaxation rate r of the spin structures due to atomic motion of $r \approx 2.8 \times 10^3 \text{ s}^{-1}$ and $r \approx 4.4 \times 10^3 \text{ s}^{-1}$, respectively (see Eqs. (19) and (20) of the Supplementary Note 1).

After the atomic sample is prepared in the MOT, the MOT is shut down by switching off both trapping lasers and magnetic field gradient. After a delay, the cloud is submitted to a pulsed retro-reflected laser beam using the configuration depicted in Fig. 1a. The duration of the pulse is typically 400 μs . The input laser beam, with a linear polarization, is detuned below the $F = 2 \rightarrow F' = 3$ transition of the D2 line of ^{87}Rb , chosen as the transition is closed. The typical detuning is $\delta = -(7 \dots 9)\Gamma$, where $\Gamma = 2\pi \times 6.06 \text{ MHz}$ is the atomic linewidth. Since the optical pumping process tends to increase the population in the stretched states with the strongest dipole matrix element, the optical density increases due to the pumping process and the optical nonlinearity is self-focusing in spite of negative detuning. The beam diameters (FWHM) of the pump beams are 2.2 mm (Nice) and 0.8 mm (Strathclyde). Depending on the laser power, a superimposed weak repumping beam tuned to the $F = 1 \rightarrow F' = 2$ transition is added to prevent hyperfine pumping. Because the spin instability is highly magnetic field-dependent, the residual B has to be carefully controlled. This is achieved by a sufficiently long delay of 3 to 10 ms between MOT shutdown and the pattern-forming laser pulse and a set of three pairs of Helmholtz coils to control the bias fields. The residual magnetic field is compensated to best effort in all three dimensions. We cannot exclude uncontrolled magnetic fields on the order of some tens of mG.

The feedback mirror is located outside the vacuum chamber and imaged with a telescope closer to the atomic sample. Hence one can achieve also negative feedback distances^{54,68}.

In Fig. 5b, the critical magnetic field used for scaling is expected to be proportional to the input intensity, $B_{crit} = \zeta I_{in}$, see Eq. (12). The scaling factor is obtained by first dividing the critical magnetic field values by the pump intensity and averaging the obtained numbers giving $\zeta = (8.7 \pm 0.1) \times 10^{-3}$ for the B_x -fields and $\zeta = (1.1 \pm 0.1) \times 10^{-2}$ for the B_y -fields.

Pattern detection and analysis. The pattern detection relies on the imaging of the transverse intensity distribution of the weak beam transmitted by the semi-transparent feedback mirror. The small amount of light transmitted by the mirror is used to image the transverse intensity distribution of the beam either in near-field (NF, at a plane located at a distance $2d$ behind the cloud corresponding to the intensity distribution fed back to the atoms) or in far-field (FF, in the focal plane of a suitably positioned lens). This imaging can be performed simultaneously in two orthogonal polarization channels (either circular (σ^+/σ^-) or linear). The NF images are employed to identify the nature of the magnetic phase. From Eq. (2) and the propagation phase shift of $\pi/2$, the difference between the transmitted intensities of the two σ -components is proportional to the magnetization w in linear order, justifying the visualization used in Fig. 3c, e, h, j. In the far field, the Fourier spectrum of the magnetic structure is available. The diffracted power used in Fig. 5a is obtained by integrating the intensity in FF images within the transverse wave number range of the structure. From Eq. (2), in linear order the field is proportional to the modulation amplitude of w at that wavenumber, whereas the recorded intensity is proportional to the square of the modulation amplitude of the magnetization. As the latter is proportional to the staggered order parameter of the antiferromagnetic state, the diffracted power is expected to indicate the square of the order parameter of the Ising model. The normalization constants for the diffracted power in Fig. 5b are obtained by fitting parabolas to the data in Fig. 5a.

Theoretical model. Equations of motion for the atomic magnetization states in the electronic ground state are derived from the Liouville equation for the density matrix. The procedure is outlined in the Supplementary Note 1. The numerical simulations are performed in the representation outlined in the Supplementary Note 1, but it is useful to note that these equations can be rewritten in terms of irreducible tensor components of rank 1 describing orientation or magnetic dipoles and components of rank 2 describing alignment components or magnetic quadrupoles, respectively, and that the magnetic field provides only a coupling within the dipole, respectively quadrupole, components, but not between tensors of different rank. The coherent dynamics of the magnetic dipole vector \mathbf{m} in the external magnetic field Ω is described by

$$\dot{\mathbf{m}} = \Omega \times \mathbf{m}, \quad (4)$$

where the z -component of the magnetization represents the orientation introduced before, $m_z = w$. As we concentrate on the dipole dynamics in this article and the m_z component is the only one directly coupling to the optical field, we proceed by neglecting the contributions from the rank 2 components and solving for the m_x , m_y components in steady state. This results in an effective equation for the orientation given by

$$\dot{w} = -\left(r + \frac{1}{6}S\right) \left[1 + \frac{\Omega_x^2 + \Omega_y^2}{\left(\frac{r + \frac{17}{24}S}{r + \frac{1}{6}S}\right)^2 + \Omega_z^2} \frac{r + \frac{17}{24}S}{r + \frac{1}{6}S} \right] w + \frac{5}{18}D, \quad (5)$$

$$= -\Gamma_w \left[1 + \frac{\Omega_x^2 + \Omega_y^2}{\left(\frac{r + \frac{17}{24}S}{r + \frac{1}{6}S}\right)^2 + \Omega_z^2} \frac{r + \frac{17}{24}S}{r + \frac{1}{6}S} \right] w + \frac{5}{18}D \quad (6)$$

which illustrates nicely the destruction of longitudinal magnetization by the transverse B-fields in addition to the decay rate Γ_w evaluated at $\Omega_x = \Omega_y = 0$. The dash in Ω_z^2 illustrates that one might need to take into account light-shift contributions for a fully quantitative description, but the spatial average of light-shift is zero as long as $\Omega_z = 0$. For $\Omega_z = 0$, Eq. (6) reduces then to

$$\dot{w} = -\Gamma_w \left[1 + \frac{\Omega_x^2 + \Omega_y^2}{\left(\frac{r + \frac{17}{24}S}{r + \frac{1}{6}S}\right) \left(r + \frac{1}{6}S\right)} \right] w + \frac{5}{18}D, \quad (7)$$

which is used to analyze the destruction of magnetic order by the transverse field in Fig. 5.

Symmetry breaking in a longitudinal magnetic field. For zero difference pump rate D , the homogeneous state of the z -magnetization is $w = 0$ from Eq. (6). A non-zero longitudinal field provides a symmetry breaking. However, the main effect does not arise directly via the dipole energy but via the chiral optical properties of the atom as light-mediated coupling is responsible for the z -magnetization. First, the difference pump rate D is different from zero even with linearly polarized input light, if the longitudinal magnetic field is nonzero, as the pump rates depend on detuning and hence on the Larmor frequency Ω_z (nonlinear Faraday effect, see Eq. (3) of Supplementary Note 1). However, the effect is small as it is linear in Ω_z/δ , $D \approx 4P_0\Omega_z/\delta$ (P_0 input pump rate for one circular polarization at $\Omega_z = 0$), and the experiments operate at $B_z \approx 0.1 \text{ G}$ and $|\delta| \approx 7.5\Gamma$ giving $|4\Omega_z/\delta| \approx 0.006$. For the same reason, the symmetry breaking provided by the linear Faraday effect, the difference in linear optical phase shift between the two σ -components (Eq. (24) of Supplementary Note 1), is small. However, for sufficiently large B_z fields one can obtain a sizable homogeneous magnetization, which corresponds to the anticipated paramagnetic state mentioned in the article. The dominant symmetry breaking for small longitudinal magnetic fields is provided by the precession term between the

coherences u and v in Eqs. (8a) and (8b) of the Supplementary Note 1. From this, a homogeneous component u_0 created directly by the linearly polarized pump beam induces a homogeneous component v_0 , which in turn couples to the z -magnetization w via a term proportional v (see Eq. (8c) of the Supplementary Note 1). As the sign of v_0 generated depends on the sign of B_z , this provides a symmetry breaking for w destabilizing the antiferromagnetic state. However, if the B_z -field is increased further, it leads to a destruction of the coherences by the precession around the B_z -field and thus to a reduction of symmetry breaking. This transition seems to be related to the transition between nicely ordered ferrimagnetic states and the disordered states mentioned. As at higher pump rate the coherence survives to larger B_z -fields, the range with nice, ordered hexagons changes being the main reason for a range of B_z mentioned in the caption of Fig. 3.

Linear stability analysis. For the linear stability analysis of the homogeneous state we confine to perturbations in the orientation w as the numerical simulations suggest that the orientation is the driver for the magnetic ordering under consideration. Hence we solve Eq. (8) of Supplementary Note 1 for the homogeneous stationary state u_0, v_0, X_0, w_0 without a transverse magnetic field and set $w = w_0 + \delta w \cos(qx)$ with a small perturbation δw at a wavenumber q . The resulting equation for the growth rate of δw in linear approximation for the wavenumber with the lowest threshold (i.e. the one of the emerging ordered state, $q_c = \sqrt{\pi k/(2d)}$) is for $\Omega_z = 0$

$$\eta = -r - \frac{1}{6}S_0(1+R) + R\left(\frac{X_0}{6} - \frac{5}{12}\right)S_0\phi_0, \quad (8)$$

where P_0 is the input pump rate for one circular component of the linearly polarized light and $S_0 = 2P_0$ and $\phi_0 = \phi_+$ ($\Omega_z = 0$) = ϕ_+ ($\Omega_z = 0$). The first term describes the destruction of ordering due to the residual atomic motion while the second term accounts for the fact that the orientation is bounded. The third term is the driving term. It is positive as $\phi_0 < 0$ for $\delta < 0$. It is reduced by the development of a homogeneous alignment X_0 . Except for this X_0 term, Eq. (8) has the same structure as the expression derived for a $J = 1/2$ -system^{44,45} but with coefficients and signs adapted to the different term scheme. The threshold pump rate is obtained as

$$S_0 = \frac{r}{-\frac{1}{6}(1+R) + \left(\frac{X_0}{6} - \frac{5}{12}\right)R\phi_0}, \quad (9)$$

giving a minimal linear phase shift to obtain ordering of

$$|\phi_0| = \frac{1+R}{6R\left(\frac{5}{12} - \frac{X_0}{6}\right)}. \quad (10)$$

For $r = 0$ (zero effective temperature, i.e. no classical fluctuations are counteracting the ordering) the pump threshold is zero (without a transverse field), but a finite optical density (phase shift) is still needed to obtain magnetic ordering. Hence, ϕ_0 is the cooperativity parameter characterizing the interaction strength. For $X_0 = 0$, i.e. considering only the dipole components, Eq. (10) indicates the requirement of a minimum phase shift of 0.82.

Turning our attention to the consequences of the presence of the higher order magnetic multipoles, numerical simulations show that X_0 varies roughly between 0.25 and 0.5. Hence, the corrections to the minimum required phase are quite small (0.91–1.03) and not very important except when the optical density is so low that the linear phase shift is close to the minimally required one. This is the case for the Strathclyde experiment which operates at $|\phi_0| \approx 0.96$. The consequences for the threshold are discussed in the final paragraph of Section ‘Threshold behavior’. For the higher density involved in the Nice experiment, $|\phi_0| \approx 2.32$ ($b_0 = 80$, $\delta = -8.6\Gamma$), the correction by X_0 is not very important. For $r = 4.4 \times 10^3 \text{ s}^{-1}$ and $R = 0.95$ one obtains $I_{\text{th}} = 0.062 \text{ mW/cm}^2$ for $X_0 = 0$ and $I_{\text{th}} = 0.076 \text{ mW/cm}^2$ for $X_0 = 0.29$.

As these differences are small, we have neglected higher order magnetic multipoles in the discussion of Fig. 5c and calculated the critical transverse field just from the tensor 1 components from Eq. (7),

$$\Omega_{\text{c,trans}}^2 = -\frac{r}{12}\left(r + \frac{17}{24}S_0(1+R)\right)RS_0\phi_0 - \left(r + \frac{17}{24}S_0(1+R)\right)\left(r + \frac{1}{6}S_0(1+R)\right), \quad (11)$$

indicating a linear relationship between critical field and pump power for $S_0 \gg r$

$$\Omega_{\text{c,trans}} = S_0 \sqrt{\frac{17}{24}(1+R) \left[-\frac{5}{12}R\phi_0 - \frac{1}{6}(1+R) \right]}. \quad (12)$$

The critical magnetic field also increases with increasing dispersive optical density ϕ_0 , i.e. increasing interaction strength.

Data availability. Data used to plot the figures are available under <https://doi.org/10.15129/386278bf-dd5f-4dd6-8808-2a2728beed93>. Further relevant data are available on reasonable request from the authors.

Received: 9 January 2018 Accepted: 8 June 2018

Published online: 10 July 2018

References

- Bloch, I., Dalibard, J. & Nascimbène, S. Quantum simulations with ultracold quantum gases. *Nat. Phys.* **8**, 267–276 (2012).
- Struck, J. et al. Quantum simulation of frustrated classical magnetism in triangular optical lattices. *Science* **333**, 996–999 (2012).
- Greif, D., Uehlinger, T., Jotzu, G., Tarruel, L. & Esslinger, T. Short-range quantum magnetism of ultracold fermions in an optical lattice. *Science* **340**, 1307–1310 (2013).
- Brown, R. C. et al. Two-dimensional superexchange-mediated magnetization dynamics in an optical lattice. *Science* **348**, 540–544 (2015).
- Labuhn, H. et al. Tunable two-dimensional arrays of single Rydberg atoms for realizing quantum Ising models. *Nature* **534**, 667–670 (2016).
- Mazurenko, A. et al. A cold-atom Fermi-Hubbard antiferromagnet. *Nature* **545**, 462–466 (2017).
- Valtolina, G. et al. Exploring the ferromagnetic behaviour of a repulsive Fermi gas through spin dynamics. *Nat. Phys.* **13**, 704–709 (2017).
- de Paz, A. et al. Nonequilibrium quantum magnetism in a dipolar lattice gas. *Phys. Rev. Lett.* **111**, 185305 (2013).
- Zeiger, J. et al. Coherent many-body spin dynamics in a long-range interacting Ising chain. *Phys. Rev. X* **7**, 041063 (2017).
- Bernien, H. et al. Probing many-body dynamics on a 51-atom quantum simulator. *Nature* **551**, 579–584 (2017).
- Zhang, J. et al. Observation of a many-body dynamical phase transition with a 53-qubit quantum simulator. *Nature* **551**, 601–604 (2018).
- Stenger, J. et al. Spin domains in ground-state Bose-Einstein condensates. *Nature* **396**, 345–348 (1998).
- Sadler, L. E., Higbie, J. M., Leslie, S. R., Vengalattore, M. & Stamper-Kurn, D. M. Spontaneous symmetry breaking in a quenched ferromagnetic spinor Bose-Einstein condensate. *Nature* **443**, 312–315 (2006).
- Liu, Y. et al. Quantum phase transitions and continuous observation of spinor dynamics in an antiferromagnetic condensate. *Phys. Rev. Lett.* **102**, 125301 (2009).
- Lin, Y.-J., Jiménez-García, K. & Spielman, I. B. Spin-orbit-coupled Bose-Einstein condensates. *Nature* **471**, 83–86 (2011).
- Ruokokoski, E., Huhtamäki, J. A. M. & Möttönen, M. Stationary states of trapped spin-orbit-coupled Bose-Einstein condensates. *Phys. Rev. A* **86**, 051607 (2012).
- Kadav, H. et al. Observing the Rosensweig instability of a quantum ferrofluid. *Nature* **530**, 194–197 (2016).
- Stuhler, J. et al. Observation of dipole-dipole interaction in a degenerate quantum gas. *Phys. Rev. Lett.* **95**, 150406 (2005).
- Elliott, R. J., Pfeuty, P. & Wood, C. Ising model with a transverse field. *Phys. Rev. Lett.* **25**, 443 (1970).
- Fogedby, H. C. The Ising chain in a skew magnetic field. *J. Phys. C Solid State Phys.* **11**, 2801–2813 (1978).
- Ovchinnikov, A. A., Dmitriev, D. V., Krivnov, V. Y. & Chervanovskii, V. O. Antiferromagnetic Ising chain in a mixed transverse and longitudinal magnetic field. *Phys. Rev. B* **68**, 214406 (2003).
- Neto, M. A. & de Sousa, J. R. Transverse Ising antiferromagnet in a longitudinal magnetic field: study of the ground state. *Phys. Lett. A* **330**, 322–325 (2004).
- Neto, M. A. & de Sousa, J. R. Phase diagrams of the transverse Ising antiferromagnet in the presence of the longitudinal magnetic field. *Phys. A* **392**, 1–6 (2013).
- Sachdev, S. *Quantum Phase Transitions* 2nd edn (Cambridge University Press, Cambridge, 2011).
- Dutta, A. et al. *Quantum Phase Transitions in Transverse Field Spin Models* (Cambridge University Press, Cambridge, 2015).
- Jozef Streečka, J. & Jaščur, M. A brief account of the Ising and Ising-like models: mean-field, effective-field and exact results. *Acta Phys. Slovaca* **65**, 235–367 (2015).
- Firth, W. J. Spatial instabilities in a Kerr medium with single feedback mirror. *J. Mod. Opt.* **37**, 151–153 (1990).
- Talbot, W. H. F. Facts relating to optical science. No. IV. *Philos. Mag.* **9**, 401–407 (1836).
- Tesio, E., Robb, G. R. M., Ackemann, T., Firth, W. J. & Oppo, G.-L. Spontaneous optomechanical pattern formation in cold atoms. *Phys. Rev. A* **86**, 031801 (2012).
- Kollar, A. J. et al. Supermode-density-wave-polariton condensation with a Bose-Einstein condensate in a multimode cavity. *Nat. Commun.* **8**, 14386 (2016).
- Domokos, P. & Ritsch, H. Collective cooling and self-organization of atoms in a cavity. *Phys. Rev. Lett.* **89**, 253003 (2002).

32. Black, A. T., Chan, H. W. & Vuletic, V. Observation of collective friction forces due to spatial self-organization of atoms: from Rayleigh to Bragg scattering. *Phys. Rev. Lett.* **91**, 203001 (2003).
33. Baumann, K., Guerlin, C., Brennecke, F. & Esslinger, T. Dicke quantum phase transition with a superfluid gas in an optical cavity. *Nature* **464**, 1301–1307 (2010).
34. Léonard, J., Morales, A., Zupancic, P., Esslinger, T. & Donner, T. Supersolid formation in a quantum gas breaking a continuous translational symmetry. *Nature* **543**, 87–90 (2017).
35. Labeyrie, G. et al. Optomechanical self-structuring in a cold atomic gas. *Nat. Photon* **8**, 321–325 (2014).
36. Greenberg, J. A., Schmittberger, B. L. & Gauthier, D. Bunching-induced optical nonlinearity and instability in cold atoms. *Opt. Express* **19**, 22535–22549 (2011).
37. Schmittberger, B. L. & Gauthier, D. J. Spontaneous emergence of free-space optical and atomic patterns. *New J. Phys.* **18**, 103021 (2016).
38. Camara, A. et al. Optical pattern formation with a two-level nonlinearity. *Phys. Rev. A* **92**, 013820 (2015).
39. Omont, A. Irreducible components of the density matrix. Application to optical pumping. *Prog. Quantum Electron.* **69–138**, 5 (1977).
40. Stöckmann, H.-J. & Dubbers, D. Generalized spin precession equations. *New J. Phys.* **16**, 053050 (2014).
41. Grynberg, G., Matre, A. & Petrossian, A. Flowerlike patterns generated by a laser beam transmitted through a rubidium cell with a single feedback mirror. *Phys. Rev. Lett.* **72**, 2379–2382 (1994).
42. Grynberg, G. Drift instability and light-induced spin waves in an alkali vapor with a feedback mirror. *Opt. Commun.* **109**, 483–486 (1994).
43. Ackemann, T. & Lange, W. Non- and nearly hexagonal patterns in sodium vapor generated by single-mirror feedback. *Phys. Rev. A* **50**, 4468–4471 (1994).
44. Scroggie, A. J. & Firth, W. J. Pattern formation in an alkali-metal vapor with a feedback mirror. *Phys. Rev. A* **53**, 2752–2764 (1996).
45. Aumann, A., Büthe, E., Logvin, Y. A., Ackemann, T. & Lange, W. Polarized patterns in sodium vapor with single mirror feedback. *Phys. Rev. A* **56**, 1709–1712 (1997).
46. Lange, W., Ackemann, T., Aumann, A., Büthe, E. & Logvin, Y. A. Atomic vapors – a versatile tool in studies of optical pattern formation. *Chaos Solitons Fractals* **10**, 617–626 (1999).
47. Grynberg, G. et al. Observation of instabilities due to mirrorless four-wave mixing oscillation in sodium. *Opt. Commun.* **67**, 363–366 (1988).
48. Firth, W. J. & Paré, C. Transverse modulational instabilities for counterpropagating beams in Kerr media. *Opt. Lett.* **13**, 1096–1098 (1988).
49. Gauthier, D. J., Malcuit, M. S. & Boyd, R. W. Polarization instabilities of counterpropagating laser beams in sodium vapor. *Phys. Rev. Lett.* **61**, 1827–1830 (1988).
50. Firth, W. J., Fitzgerald, A. & Paré, C. Transverse instabilities due to counterpropagation in Kerr media. *J. Opt. Soc. Am. B* **7**, 1087–1097 (1990).
51. Petrossian, A., Pinar, M., Maître, A., Courtois, J. Y. & Grynberg, G. Transverse pattern formation for counterpropagating laser beams in rubidium vapour. *Europhys. Lett.* **18**, 689–695 (1992).
52. Dawes, A. M. C., Illing, L., Clark, S. M. & Gauthier, D. J. All-optical switching in rubidium vapor. *Science* **308**, 672–674 (2005).
53. Dawes, A. M. C. et al. Transverse optical patterns for ultra-low-light-level all-optical switching. *Laser Photon. Rev.* **4**, 221–243 (2010).
54. Firth, W. J., Krešić, I., Labeyrie, G., Camara, A. & Ackemann, T. Thick-medium model of transverse pattern formation in optically excited cold two-level atoms with a feedback mirror. *Phys. Rev. A* **96**, 053806 (2017).
55. Busse, F. H. Non-linear properties of thermal convection. *Rep. Prog. Phys.* **41**, 1929–1967 (1978).
56. Cross, M. C. & Hohenberg, P. C. Pattern formation outside of equilibrium. *Rev. Mod. Phys.* **65**, 851–1112 (1993).
57. Gollwitzer, C., Rehberg, I. & Richter, R. From phase space representation to amplitude equations in a pattern-forming experiment. *New J. Phys.* **12**, 093037 (2010).
58. Toulouse, G. Theory of the frustration effect in spin glasses: I. *Commun. Phys.* **2**, 115–119 (1977).
59. Kaneyoshi, T. Ferrimagnetism in a transverse Ising antiferromagnet. *J. Magn. Magn. Mater.* **406**, 83–88 (2016).
60. Kushwaha, P., Rawat, R. & Chaddah, P. Metastability in the ferrimagnetic–antiferromagnetic phase transition in Co substituted Mn_2Sb . *J. Phys. Condens. Matter* **20**, 022204 (2008).
61. Yusuf, S. M., Thakur, N., Medarde, M. & Keller, L. Magnetic field driven transition from an antiferromagnetic ground state to a ferrimagnetic state in $\text{Rb}_0.19\text{Ba}_0.3\text{Mn}_1.1[\text{Fe}(\text{CN})_6] \cdot 0.48\text{H}_2\text{O}$ Prussian blue analogue. *J. Appl. Phys.* **112**, 093903 (2012).
62. Mondaini, R., Fratus, K. R., Srednicki, M. & Rigol, M. Eigenstate thermalization in the two-dimensional transverse field Ising model. *Phys. Rev. A* **93**, 032104 (2016).
63. Strack, P. & Sachdev, S. Dicke quantum spin glass of atoms and photons. *Phys. Rev. Lett.* **107**, 277202 (2011).
64. Vasin, M., Ryzhov, V. & Vinokur, V. M. Quantum-to-classical crossover near quantum critical point. *Sci. Rep.* **5**, 18600 (2015).
65. Tlidi, M., Mandel, P. & Lefever, R. Localized structures and localized patterns in optical bistability. *Phys. Rev. Lett.* **73**, 640–643 (1994).
66. Firth, W. J. & Scroggie, A. J. Optical bullet holes: robust controllable localized states of a nonlinear cavity. *Phys. Rev. Lett.* **76**, 1623–1626 (1996).
67. Tesio, E., Robb, G. R. M., Ackemann, T., Firth, W. J. & Oppo, G.-L. Dissipative solitons in the coupled dynamics of light and cold atoms. *Opt. Express* **21**, 26144–26149 (2013).
68. Ciaramella, E., Tamburrini, M. & Santamato, E. Talbot assisted hexagonal beam patterning in a thin liquid crystal film with a single feedback mirror at negative distance. *Appl. Phys. Lett.* **63**, 1604–1606 (1993).

Acknowledgements

The Strathclyde group is grateful for support by the Leverhulme Trust, the collaboration between the two groups is supported by the Royal Society (London), the CNRS, in particular the Laboratoire international associé (LIA) ‘Solace’, and the University of Strathclyde. The Nice group acknowledges support from CNRS, UNS, and Région PACA. The final stage of this work was performed in the framework of the European Training Network ColOpt, which is funded by the European Union (EU) Horizon 2020 program under the Marie Skłodowska-Curie action, grant agreement 721465.

Author contributions

I.K., P.M.G., P.G. (Strathclyde), and G.L. (Sophia-Antipolis) performed the experiments. They were joined by T.A. and R.K. in data analysis. I.K., G.R., T.A., and G.L.O. performed the theoretical and computational analysis. T.A. conceived the experiments and coordinated the efforts. All authors contributed to the discussion and interpretation of results and commented on the manuscript.

Additional information

Supplementary Information accompanies this paper at <https://doi.org/10.1038/s42005-018-0034-3>.

Competing interests: The authors declare no competing interests.

Reprints and permission information is available online at <http://npg.nature.com/reprintsandpermissions/>

Publisher's note: Springer Nature remains neutral with regard to jurisdictional claims in published maps and institutional affiliations.



Open Access This article is licensed under a Creative Commons Attribution 4.0 International License, which permits use, sharing, adaptation, distribution and reproduction in any medium or format, as long as you give appropriate credit to the original author(s) and the source, provide a link to the Creative Commons license, and indicate if changes were made. The images or other third party material in this article are included in the article's Creative Commons license, unless indicated otherwise in a credit line to the material. If material is not included in the article's Creative Commons license and your intended use is not permitted by statutory regulation or exceeds the permitted use, you will need to obtain permission directly from the copyright holder. To view a copy of this license, visit <http://creativecommons.org/licenses/by/4.0/>.

© The Author(s) 2018